Hybrid Monte Carlo and deterministic simulation approach for modeling a computed radiography imaging chain from X-ray exposure to optical readout

Min Yao, Valerie Kaftandjian, Angéla Peterzol-Parmentier, Andreas Schumm, Philippe Duvauchelle

Accepted Manuscript

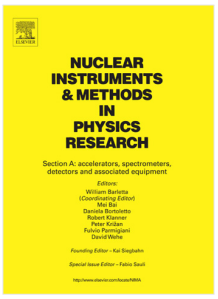

Hybrid Monte Carlo and deterministic simulation approach for modeling a computed radiography imaging chain from X-ray exposure to optical readout

Min Yao, Valérie Kaftandjian, Angéla Peterzol-Parmentier, Andreas Schumm, Philippe Duvauchelle

PII: S0168-9002(19)30914-3
DOI: https://doi.org/10.1016/j.nima.2019.06.069
Reference: NIMA 62328

To appear in: *Nuclear Inst. and Methods in Physics Research, A*

Received date : 25 July 2018
Revised date : 23 May 2019
Accepted date : 29 June 2019

Please cite this article as: M. Yao, V. Kaftandjian, A. Peterzol-Parmentier et al., Hybrid Monte Carlo and deterministic simulation approach for modeling a computed radiography imaging chain from X-ray exposure to optical readout, *Nuclear Inst. and Methods in Physics Research, A* (2019), https://doi.org/10.1016/j.nima.2019.06.069

Hybrid Monte Carlo and deterministic simulation approach for modeling a computed radiography imaging chain from X-ray exposure to optical readout

Min YAO[a], Valérie Kaftandjian[a], Angéla Peterzol-Parmentier[b], Andreas Schumm[c]
Philippe Duvauchelle[a,]

[a] Laboratoire Vibrations Acoustique (LVA) INSA Lyon, 25, Av. Jean Capelle - 69621 Villeurbanne Cedex, France
[b] Framatome / Intercontrôle 04, Rue Thomas Dumorey, 71200 Chalon sur Saone France
[c] EDF – R&D, Département Matériaux et Mécanique des Composants, EDF LAB Les Renardières – ECUELLES, 77818 Moret-sur-Loing Cedex, France

Abstract: Simulation of radiographic inspection is of great interest for experimental outcomes prediction and optimal operating condition determination. As concerns computed radiography (CR), the use of photo-stimulable imaging plates and laser scanners, implies modeling the behavior of a multi-stages detector. As a consequence, both the X-ray and the optical system responses have to be handled. Moreover, for high energy X-rays, two issues often trouble CR simulation: long running time and X-ray scattering image contribution, which should not be neglected. To overcome these issues, we have developed a complete hybrid model which is the first available one at such energies. In our approach, the imaging process is decomposed into three independent successive stages: X-ray attenuation by an object, X-ray latent image generation, and optical readout. A deterministic code is applied to obtain rapidly the transmitted X-ray image emerging from a complex object. The energy deposition is then simulated by a convolution of the transmitted X-ray image with a CR detector response model, which was obtained off-line by a Monte Carlo tool. Then, optical readout is modeled using the same hybrid approach, where the optical response (laser light spreading in the imaging plate) was obtained by Monte Carlo and laser scanning is modeled analytically. A good agreement has been observed between the proposed hybrid model and a full Monte Carlo approach for the X-ray energy deposition stage. A realistic X-ray inspection case study has been chosen to emphasize the interest of this complete hybrid model. The comparison of three different detector configurations and the influence of readout laser power are illustrated.

Keywords : Computed Radiography, Imaging Plate, Monte Carlo simulation, deterministic simulation, optical readout modelling

1 Introduction

For over a century, film-based radiography has been used for industrial inspection. Recently, the NDT community started considering alternative digital techniques [1]. Computed radiography

(CR), as the first standardized digital radiographic imaging technique, is an interesting alternative [2], as it employs a flexible (i.e. which can be bent and cut) storage phosphor imaging plate (IP) as digital detector, which shares the same advantages in terms of handling as film. However, the performance of standard CR systems is not as good as film-based radiography at high energies (i.e. several hundred keV up to MeV). For the inspection of high attenuation specimens (e.g. pipeline welding), high energy gamma sources, such as isotopes Iridium-192 and Cobalt-60, are often required. Therefore, the unsatisfied CR performance at high energies is an issue to be overcome in industrial applications.

The performance improvement of CR can be achieved by means of introducing appropriate filters and thin metallic screens in the system. Current international standards, concerning NDT radiography with digital detectors, address general metallic screen employment guidelines to ensure a good imaging quality [2-4]. However, the type and thickness of such screens are not clearly defined and a large panel of possible configurations does exit. Experimental studies on the CR image quality [1,5-7], indicate that CR cannot fulfill the requirements in all NDT cases, due to the IP response and optical readout process.

Apart from experimental studies, computational simulation is also an important tool for physical phenomena comprehension and system performance optimization [8-9]. It makes it possible to study how the relevant operating parameters affect the X-ray image without actually testing it in real life. At present, Monte Carlo and deterministic techniques are widely used to simulate radiation transport. Monte Carlo simulation is well accepted as the most accurate method [10]. It can give insight on physical phenomena but due to its random nature, a large amount of computational time is required, especially for complex geometry simulation [9-10]. Deterministic methods, on the other hand, can handle easily complex geometries, and are quite computationally efficient, but the estimation of scattering and fluorescence effects is quite difficult.

In prior works, many CR modeling and simulation studies were dedicated to medical applications [11-20]. Vedantham and Karellas have developed a complete (from X-ray exposure to digital readout) analytic CR model to analyze the system performance factor propagation during image formation process such as detective quantum efficiency (DQE) and modulation transfer function (MTF) [11]. This model is based on a cascaded linear system approach [17,18], and based on the assumption that the X-ray scattering effect is negligible. However, for high energy CR, where the scattering effect becomes dominant, this assumption is not appropriate. A more precise model is needed for scattering effect estimation. In [19] and [20], E.M. Souza et al. proposed a methodology for computed radiography simulation for industrial applications using Monte Carlo code MCNPX, taking into account the energy-dependent response of imaging plate (IP) and the digitization effect. But in their approach, the spatial degradation due to X-ray interaction in the detector has not been considered. Full Monte Carlo simulation could be the solution to overcome the mentioned issues. However, due to its random nature, the computation time might be extremely long.

In this paper, we propose a CR model which combines the use of both Monte Carlo and deterministic codes. Such a complete hybrid model is the first available one to our knowledge. The CR imaging process is split into three successive stages: i) X-ray attenuation by the object; ii) energy deposition resulting in X-ray latent image generation; iii) optical readout resulting in the final digital image generation. The first stage is based on a deterministic code which provides a realistic radiant image of a complex-shape object in a short time (typically 0.1 s) based on the object CAD model. The second stage is based on an offline CR detector response model which is obtained by means of off-line MC simulations accounting for all physical effects such as fluorescence, scattering and electrons interactions. The response function is then convolved with the object radiant image. A database of several detector systems has been built in order to cover all the industrial application range. As concerns the optical readout (third stage), the laser spreading distribution function is obtained off-line by a dedicated optical MC tool developed on purpose, while the laser scanning operation is modeled by an analytic function. Thus, we obtain a complete model which is able to simulate a realistic inspection case study in a reasonable time, while taking into account all physical effects both for X-ray and optical photons effects. It is worth noting that the presented model allows to determine mean values and obviously does not include noise. This approach allows to add noise afterwards while keeping a reasonable computation time, even for a complex shape object. Thus, all Monte Carlo simulations are carried out off-line, allowing to model all physical effects in the form of response functions.

In the following, the CR principle is briefly reminded in section 2, together with an overview of the model, then a detailed description of the different simulation stages is given in section 3. Section 4 and 5 show some results, before concluding in section 6.

2 CR principle and general overview of the modelling approach

2.1 CR principle

As illustrated in Figure 1a, CR imaging consists first in the X-ray exposure itself (A), where the energy transmitted by an object is deposited in the detector. The particularity of CR yields in the type of detector, a photo-stimulable imaging plate (IP), in which the deposited energy allows to create electron/hole pairs in the material. Some of these charges are trapped in the material, forming a latent image which is stable during several hours. The second step (B) consists of reading this latent image. A laser beam allows to excite the storage centers and light is emitted (photo-stimulation mechanism). The third step is the erasure of the plate which makes the detector available for a new image (C).

Only some specific materials present this photo-luminescence effect with sufficient stability of the trapped electrons yielding a useful latent image. The most common material is $BaFBr:Eu^{2+}$,

available in the form of grains in a binder. Since the discovery of the photo-stimulability of $BaFBr:Eu^{2+}$, several works have been done attempting to find out the physical mechanisms occurring during X-ray radiation. Present day's well accepted electron/hole production mechanism is proposed by Koschnick et al. [21,22]. It is worth noting however that those mechanisms are extremely complex and not fully understood.

$BaFBr:Eu^{2+}$ imaging plates are successfully used in the medical field, because the X-ray energy range gives rise mainly to photoelectric effects in the material. For higher energies (such as Cobalt or Iridium sources), the efficiency of imaging plates is known to be poor. To improve performances, NDT standards [2] require the use of metallic screens to be used together with IP (front and back screens), such as what is done for radiographic films. However, unlike films where the use of screens yields sufficient imaging performance at high energy, in CR, the optimal nature and thickness of screens is still to be found, such as optimal properties of the IP itself. This is the reason why simulation can be interesting, to understand the physical mechanisms during image formation, and find optimal combinations of IP/screens.

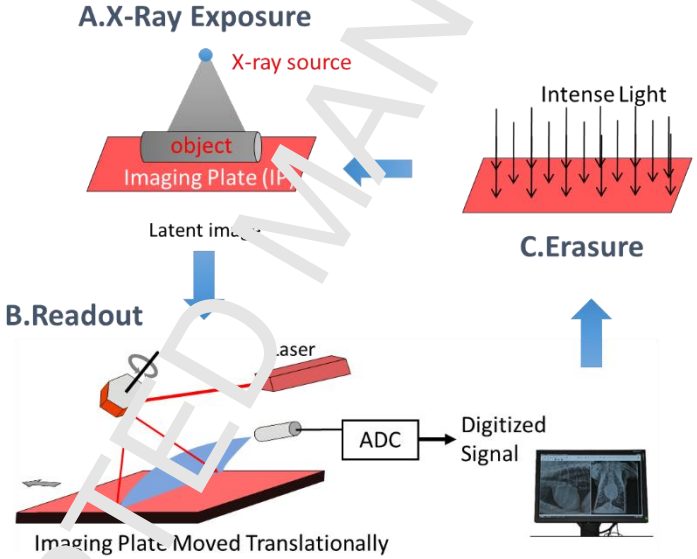

(a)

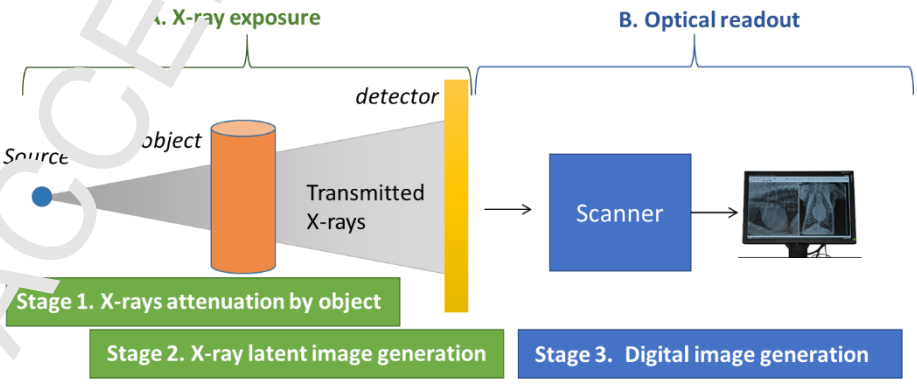

(b)

Figure 1: (a) CR principle with the acquisition procedure highlighted: A. X-ray exposure which yields a latent image, B. Optical readout of the latent image, and C. Erasure of the image; (b) only part A and B are simulated, sub-divided into three stages.

2.2. Overview of the simulation approach

During X- or gamma-ray exposure, the radiation beam first interacts with the object, and owing to the object attenuation, only part of the beam can arrive at the CR detector[1]. This transmitted beam carries the object pattern, which is received by the CR detector; a portion of the transmitted beam penetrates through the detector and escape from the system, while the other portion interacts with the detector resulting in a latent image. The CR image formation is viewed as a three-stage process (Figure 1b): X-ray attenuation, latent image generation and digital image generation. Different simulation methods (Monte Carlo or deterministic) are applied to different stages. The CR simulation method is summarized as follows.

Stage 1: X-ray attenuation by an object (X-ray beam → attenuated X-ray beam). In this step, the source beam interacts with an object resulting in an object image. In this paper, the Virtual X-ray Imaging (VXI) software, a deterministic code for fast complex imaging [23], [24], is used. The output image should contain the energy information, namely a spectral image, here denoted *Obj(E,x,y)*.

Stage 2: X-ray latent image generation (X-ray photons incoming the CR detector → storage centers in IP). This stage is split into two sub-steps.

(a) X-ray/detector interaction (X-ray photons incoming the detector → deposited energy in IP), via the detector response model (denoted PSF_{det}) resulting in a 3D deposited energy image. The detector response model is obtained by means of an off-line Monte Carlo simulation.

(b) Latent image formation (deposited energy in IP → storage centers in IP). The latent image is in fact the map of storage center distribution in IP. At present day, the latent image formation mechanism is not clearly understood. Hence this step is modeled as conversion factor, denoted g_{sc}.

The entire Stage 2 is modeled by a convolution-based operator *H1*:

$$Li\,ng(x,y,z) = H1(Obj;\ PSFdet) \qquad \textbf{(1)}$$

Stage 3: Digital image generation (storage centers → gray levels). This stage is also split into two sub-steps.

(a) Optical readout (storage centers → photo-stimulated luminescence (PSL) photons). In CR, the latent image is readout by a scanning laser. Due to the IP's granular property, the laser light spreads out in IP; storage centers within the laser volume can be released resulting in PSL. The laser spreading is simulated with a Monte Carlo tool developed on purpose. This tool outputs a laser distribution function *f(x,y,z)*. The scanning is then modelled analytically, based on the scanning parameters i.e. laser power P_{laser}, scanning speed v_{scan} and pixel size l_{pxl}.

(b) Signal collection, amplification and digitization (PSL photons → gray levels).

[1]In the following, the term "detector" should be understood as the complete system including the IP itself and front and back screens, which are metallic screens as recommended in the international standards.

In this sub-step, the emitted PSL is collected by a light guide, then detected and amplified by a photo-multiplier tube and finally digitized with an analog-to-digital converter. A PSL to gray level conversion factor g_{psl} can be applied.

Stage 3 is modeled by an operator *H2*:

$$Dimg(x,y) = H2(Limg; f; scanning\ parameters) \quad \textbf{(2)}$$

To summarize, as represented in Figure 2, the presented method allows to simulate the complete CR imaging chain, in which all the operating parameters such as source, detector configuration and optical readout parameters are taken into account through the operators *H1* and *H2*.

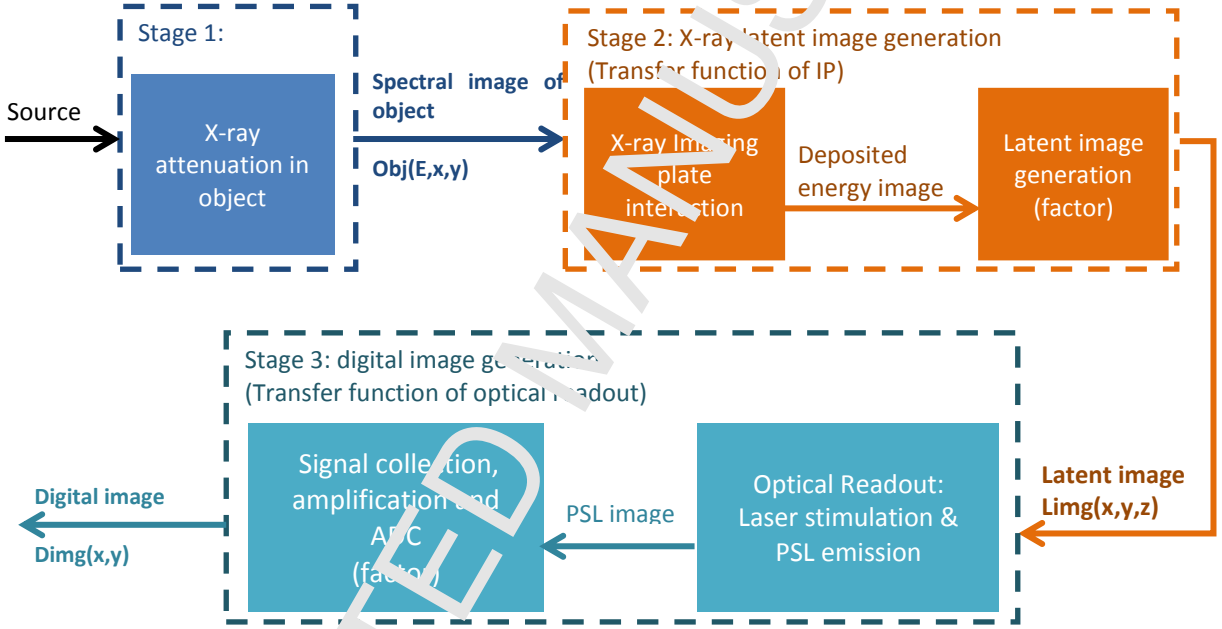

Figure 2: Schematic representation of the simulation of the entire CR imaging chain

Before introducing the details of the model, let's introduce the assumptions adopted:

- As concerns the X-ray exposure, the CR detector is considered as a linear system, so that the convolution operator H1 can be applied to obtain the X-ray detector response to any object spectral image *obj*.
- The electrons emerging from the object are neglected. Our approach deals with high attenuation object (i.e. high thickness); therefore, the fraction of electrons in the radiation emerging from the object is very small. Moreover, before arriving at the detector, a great part of the electrons are absorbed by air and cassette (normally the CR detector is handled in a cassette). Be aware that the electrons produced by metallic screens and IP are not neglected, and are taken into account in the detector model obtained by MC simulations.

- Normal incidence of radiation on the detector. In reality, the transmitted X-ray photons arrive at the CR detector with a certain incident angle. In our model, we assume the X-ray photons travel forwardly, with a normal incidence on the detector.
- Normal incidence of laser beam on the imaging plate during the readout process.

3 Detailed description of the model

3.1 Object image generation (spectral image)

In this step, to generate *Obj(E,x,y)*, a deterministic code for simulating complex imaging set-up is preferred since it can offer a realistic object image in a short time.

To generate *Obj(E,x,y)*, a virtual detector is used and placed at the actual detector plane. This virtual detector is divided into M×N pixels to record the spatial distribution of the incident photons. Each pixel pitch counts the incident photon number, and classifies the photons into different energy channels. The direct output of this virtual detector is the photon number per energy channel per pixel pitch, and the *Obj(E,x,y)* should be the output value divided by the pixel pitch surface. Figure 3 is an example of the object image generation: (a) is a geometry set-up generated using VXI software [23,24], where a virtual detector (in green) is placed at the actual detector plane; and (b) is the spectral image detected by the virtual detector *Obj(E,x,y)*.

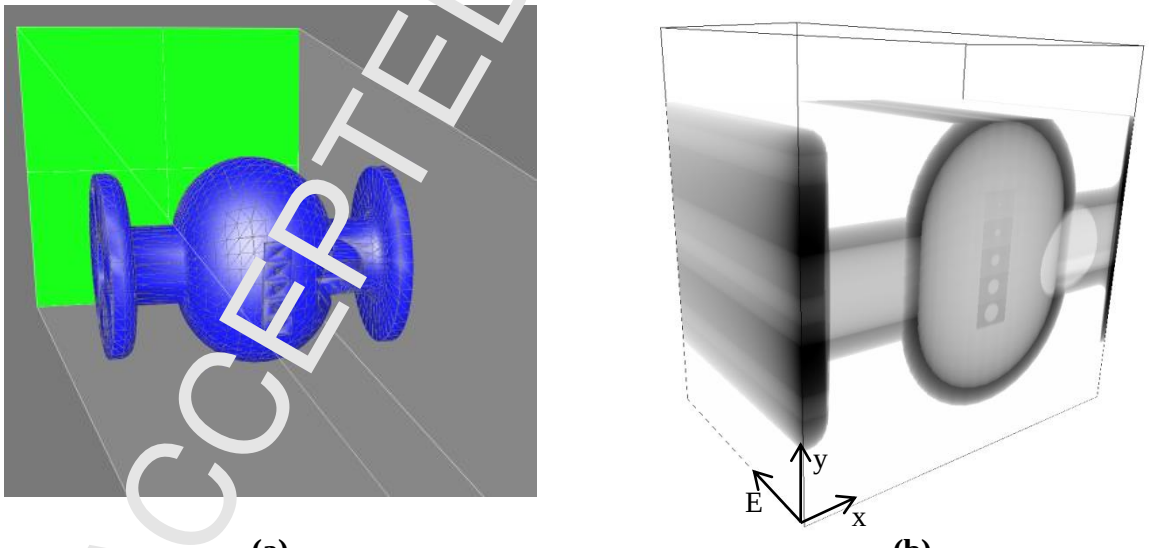

(a) **(b)**

Figure 3: Spectral object image: (a) geometry setup and (b) illustration of a spectral image. The example here is obtained with VXI software [23, 24]

3.2 Detector dose response model generation

The detector dose response model, denoted $PSF_{det}(E,x,y,z)$, is the second input required by the operator *H1*.

The detector considered in this study is a multiple-layered structure, in which the imaging plate is sandwiched between metallic screens (Figure 4a). The imaging plate also consists of multiple layers such as overcoat and phosphor layer. The phosphor layer is the effective medium which stores the latent image, and will be later readout by CR scanner. Hence the *PSF* here is a 3D energy absorption efficiency map within the IP's phosphor layer. A Monte Carlo simulation tool [25], based on the use of PENELOPE [26], has been developed to characterize the CR detector response at different energies. In order to record the *PSF*, a uniform three-dimensional grid is applied to the phosphor layer. As shown in Figure 4a, we send a mono-energetic pencil beam (E_i) to strike the detector *det*. The raw output *DEP(x,y,z)* of the simulation is illustrated in Figure 4b, which is the deposited energy map (absorbed energy per unit volume keV·cm^{-3}) within the phosphor layer. The *PSF* is obtained with:

$$PSF_{det,E_i}(x,y,z) = \frac{DEP(x,y,z)}{N_i \cdot E_i} \quad \textbf{(3)}$$

where N_i is the number of the incident photons. As a Monte Carlo calculation contains statistical noise, the incident photon number should be as large as possible to limit this noise. The impulse response is of cylinder symmetry around *z*-axis, hence we also apply a radial averaging to the *PSF* to reduce the noise, and the *PSF* is reduced to a 2D function.
In such a way, the storage space can be saved. The storage digits can be further reduced by applying an analytic fitting function to each 1D profile at different *z*.

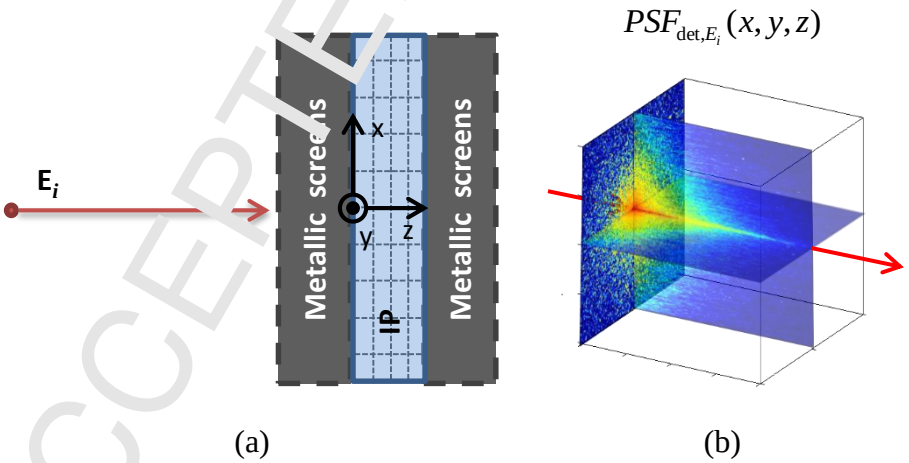

(a) (b)

Figure 4: Impulse response of a detector: (a) Geometry configuration and, (b) 3D energy deposition map: the red arrow indicates the beam propagation direction which is also the IP depth direction.

The second step of detector response model generation is to repeat the previous operations (i.e. raw *PSF* simulation and radial averaging) by scanning all energies (see Figure 5). Different

energies ranging from E_{min} to E_{max} are sampled to excite the detector *det*. After the radial averaging operation, we have a set of PSF, and all these PSFs make up the response model of the detector *det*. In order to cover the energy range of common NDT radiation sources (such as Ir192 and Co60), E_{min} is assigned 0 keV, and E_{max} 1400 keV.

In order to build a database of detector models, several detector configurations have been simulated. At present, we have covered all the metallic screens (front/back) combinations proposed in the standards EN ISO 16 371-2 [2] and ISO1763 -2 [3] as well as other screens, for different thicknesses and properties of BaFBr imaging plates to form a database of 128 configurations.

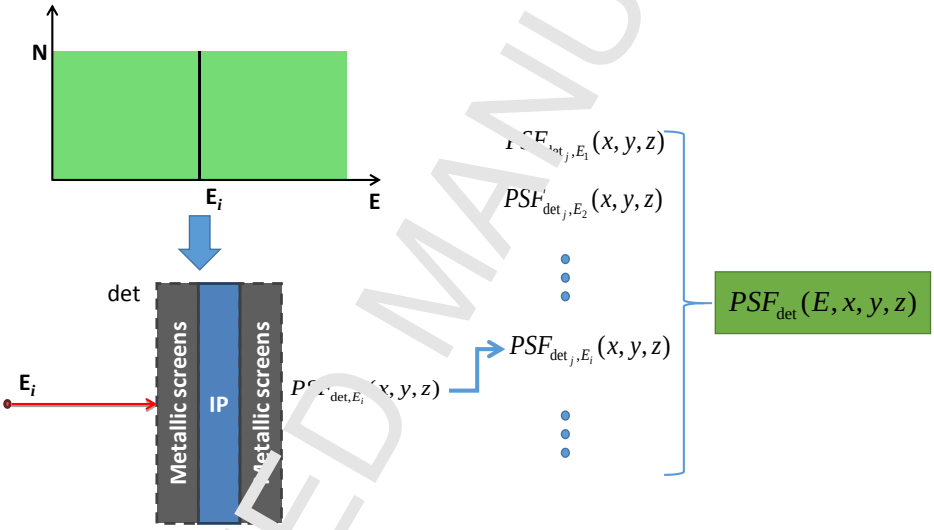

Figure 5: Generating the detector dose response function of a fixed detector *det*.

3.3 Latent image computation

The latent image generation involves the energy deposition and storage center formation. Only a portion of the deposited energy is stored in the form of storage centers. At present day, the storage center forming mechanism is still not clearly understood [27–29]; moreover, it is different from one to another material. Therefore, the latent image (storage center) formation process is simply modeled as a conversion factor g_{sc} (unit: keV^{-1}). In the review of Rowlands[28], the absorbed X-ray energy to storage center ratio in BaFBr is 2.4 keV^{-1}; while in [29], a different ratio 7.98 keV^{-1} is reported. In the following, we assign the normalized value 1 keV^{-1} to g_{sc}.

Equation (4) gives the operation realized.

$$Limg(x,y,z) = H1(Obj, PSF_{det})$$
$$= g_{sc} \int_E \left(E\ Obj(E,x,y) * PSF_{det}(E,x,y,z)\right) dE \quad \textbf{(4)}$$
$$= g_{sc} \int_E E \left(\iint_{u,v} Obj(E,u,v)\ PSF_{det}(E,x-u,y-v,z)\, du dv \right) dE$$

where:

- *H1* represents the latent image generation model which is a 2D spatial convolution (along *x* and *y*), at a given depth *z*, integrated over all energies and finally multiplied by the conversion factor g_{sc};
- gsc represents the absorbed X-ray energy to storage center conversion efficiency (unit: keV^{-1});
- *Obj(E,x,y)* is the spectral object image, namely the number of photons per unit surface per energy channel (unit: cm^{-2} . keV^{-1});
- $PSF_{det}(E,x,y,z)$ is the detector model, which is in fact a set of point spread functions (unit: cm^{-3}) for all energies;
- *E* is the X-ray photon energy (unit: keV).

The term which is multiplied by g_{sc} represents the deposited energy distribution (unit: keV. cm^{-3}). Multiplying by g_{sc} allows to convert this energy into a storage center distribution i.e. latent image.

Numerically, this equation is realized energy by energy. For each energy channel, we compute the storage center distribution at different z; by summing the latent images obtained for all energy channels, we get the final output latent image.

The corresponding computation algorithm is:

Initialize the latent image array *Limg(x,y,z) = 0*.
for *each energy channel Ei =0 to Emax* **do**
  for *each IR depth: zj = 0 to d* **do**
    Compute the latent image at depth *zj* given by photons of energy *Ei*
    $\Delta Limg(x,y,zj) = g_{sc}$ *.[*$Obj_{Ei}(x,y)$ * $PSF_{Ei,zj}$ *(x,y)]*;
    Accumulate *ΔLimg(x,y)* to the corresponding depth slice *zj* in latent image array
    Limg(x,y,zj) = Limg(x,y,zj) + ΔLimg(x,y,zj).
  end
end

Note that the numerical convolution requires the pixel size matching between *Obj* and PSF_{det}. In this paper, the sampling match is achieved by means of interpolation.
The algorithm output is a 3D latent image. We keep the information along detector depth (*z*) direction, because the latent image is read by a scanning laser, the laser power modifies the

penetration of the laser light, and thus the deep storage centers have less contribution to the readout image. With this in mind, we choose to keep the information along z.

3.4 Optical readout

Readout is a crucial process that affects the final image quality (e.g. efficiency, contrast and spatial resolution). As shown previously in Figure 1a, the basic principle of CR readout is the "flying spot": via a rotating mirror, the finely focused stimulating laser beam scans horizontally the imaging plate (IP). Together with a continuous translation of IP, the stored information can be released line by line through the whole imaging plate. This scanning process is usually called raster scan (or raster scanning).

The imaging plate has a multiple-layered structure which basically consists of a protective layer, a photo-stimulable phosphor (PSP) layer (the phosphor grains are embedded in polymer binder) and a support layer. Sometimes, a reflective or an absorbing layer is added between PSP layer and support layer. Concerning the optical readout simulation, we are only interested in the PSP layer and the two layers in contact with it. The reason is that the optical photons are much less energetic comparing with X- or γ-rays, thus the effects of the 'outer layers' can be neglected. Therefore in this part, we simulate the light transport problem in a three-layered structure (see Figure 6): top layer (e.g. protective layer), PSP layer and bottom layer (e.g., reflective layer or support layer). The top and bottom layers are considered to be clear media where the laser light travels in a straight line, while the PSP layer is modeled as granular layer where the scattering effect is pronounced.

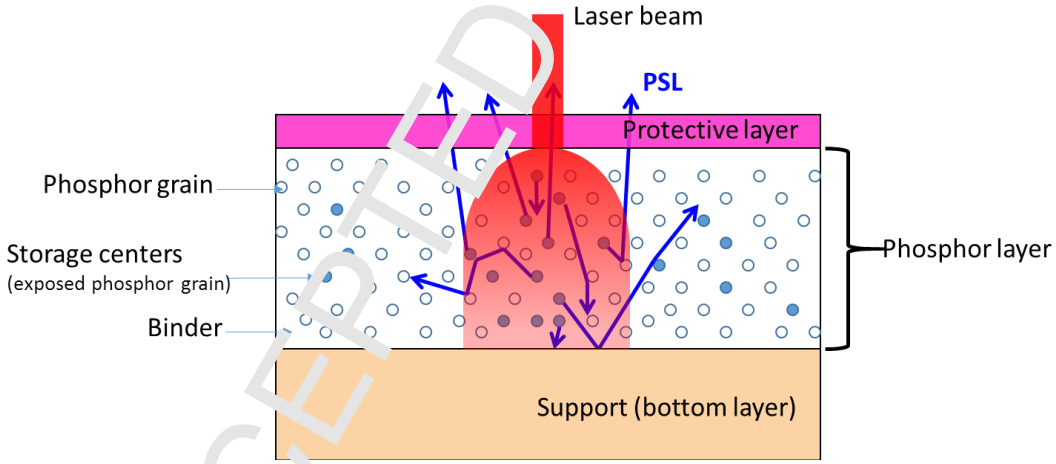

Figure 6: Optical effects within imaging plate. A three-layered structure is considered: a top layer, a PSP layer and a bottom layer, where the top and bottom layer are clear media, and the PSP layer is granular. The laser beam (red) strikes perpendicularly the front side of IP; it first passes through the top layer without expanding the beam size; in the PSP layer, the laser light diffuses along its traveling path; at the interfaces, top-PSP and PSP-bottom, the laser photons might be absorbed or reflected. Part of the storage centers within the red volume will be stimulated by laser photon resulting in PSL (blue arrows), which also suffers multiple scattering effect; only a fraction of the emitted PSL could reach the front surface and be detected contributing to the final image

The optical readout process is viewed as a transfer function H2 (Figure 7a), which also requires two inputs: latent image and IP optical response model. Flying spot scanner is the most common CR reader: a finely focused laser is used to scan and release, line by line, the latent image; the latent image is modified while the laser spot traverses the IP [22]. Thus, unlike the previous operator *H1*, *H2* is a modified convolution operation. The final digital image is computed using the following equation, where x_m, y_n denotes the coordinates of pixel m,n in the image (x and m refering to the laser scan direction, while y and n to the IP translation direction):

$$Dimg(x_m, y_n) = H_2(Limg, f, scanning\ parameters) = \int_z P(z)dz \iint_{x,y} Limg^{(m,n)}(x,y,z)\{1-\exp[-\sigma \cdot f(x-x_m, y-y_n, z) \cdot P_{laser} t_{scan}]\}dxdy \quad (5)$$

where $Limg^{(m,n)}(x,y,z)$ is the scanning modified latent image at reading point (x_m,y_n), whose formula is given in relation (6). $f(x,y,z)$ is the IP optical impulse response to a laser beam, $P(z)$ is the probability that a photon (emitted at z) could escape from the front side of IP, σ is the optical cross section of photo-stimulation, P_{laser} is the laser power and t_{scan} is the dwell time of laser spot at (x_m,y_n). This formula (5) is based on the laser-latent image interaction model in the work of Thoms [30].

The IP optical response model $f(x,y,z)$ is again obtained through the Monte Carlo method. A specific Monte Carlo code has been programmed on purpose in Matlab to simulate the light propagation problem in IP [31]. Some physical models of light/IP interaction adopted in the code are based on [32] and [33]. Figure 7b shows an example of IP response to a normal incident laser beam, for which 2×10^6 photons have been generated to strike the imaging plate.

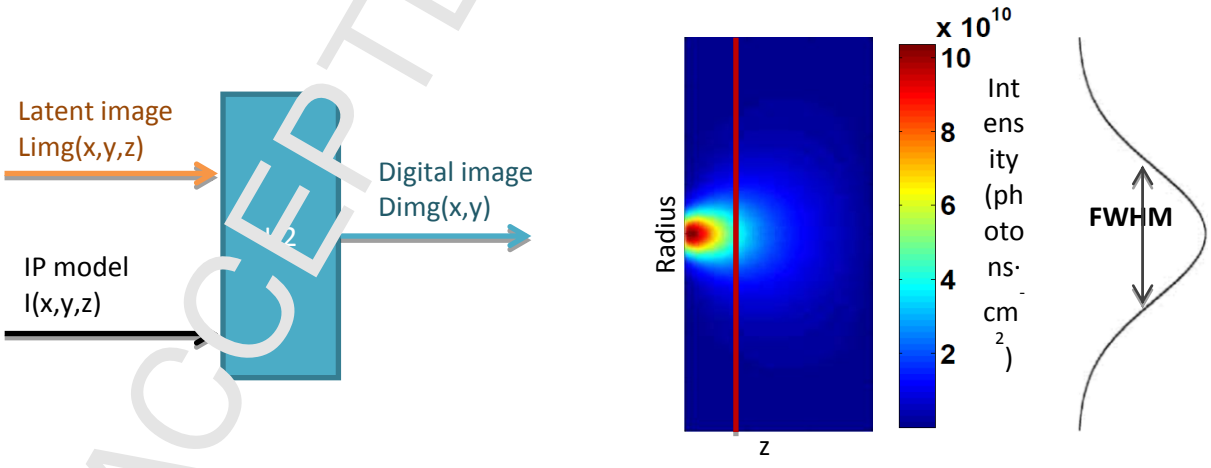

(a) (b)

Figure 7: a) Generation of the digital image using the optical readout transfer function H2; b) an example of IP model (impulse response of IP to laser light).

It is worth noting that the value of $Limg^{(m,n)}(x,y,z)$ is modified by the laser scanning process, i.e. it is changed while the laser spot moves from one position to another. For this reason, we

emphasize that $Limg^{(m,n)}(x,y,z)$ here refers to the storage center distribution right *before* the laser beam arrives at pixel *(m, n).* In order to obtain $Limg^{(m,n)}(x,y,z)$, namely the scanning modified latent image at reading point (x_m,y_n), the following formula is applied. More details can be found in [31].

$$Limg^{(m,n)}(x,y,z) = Limg(x,y,z)exp\left\{-\left[\sum_{j=0}^{n-2}\sum_{i=0}^{M-1} f\left(x-i\cdot l_{pxl}, y-j\cdot l_{pxl}, z\right) + \sum_{k=0}^{m-1} f\left(x-k\cdot l_{pxl}, y-(m-1)\cdot l_{pxl}, z\right)\right] k_{laser} t_{scan}\cdot\sigma\right\} \quad (6)$$

with l_{pxl} being the optical readout output pixel size.

The corresponding computation algorithm is:

Initialize the digital image array $Dimg(x,y) = 0$.
for *each line: n = 1 to N* **do**
  for *each pixel: m = 1 to M* **do**
    Update the latent image $Limg^{(m,n)}(x,y,z)$
    Compute the output signal of the current pixel $Dimg(x_m,y_n)$
  end
end

4 Comparison with full Monte Carlo simulation

Monte Carlo method is commonly considered as the reference for radiation transport simulation. The MC simulation package PENELOPE [26] containing detailed physical models of both x-ray/matter and charged particle/matter interactions, is used here. Since it takes into account all kinds of interactions, the simulation running is slow. As a first step to validate our model, we have chosen a very simple imaging set-up to compare the simulation results obtained with a full Monte Carlo code and our model, comparing only the X-ray exposure part (i.e. without the optical readout), in order to validate the H1 operator.

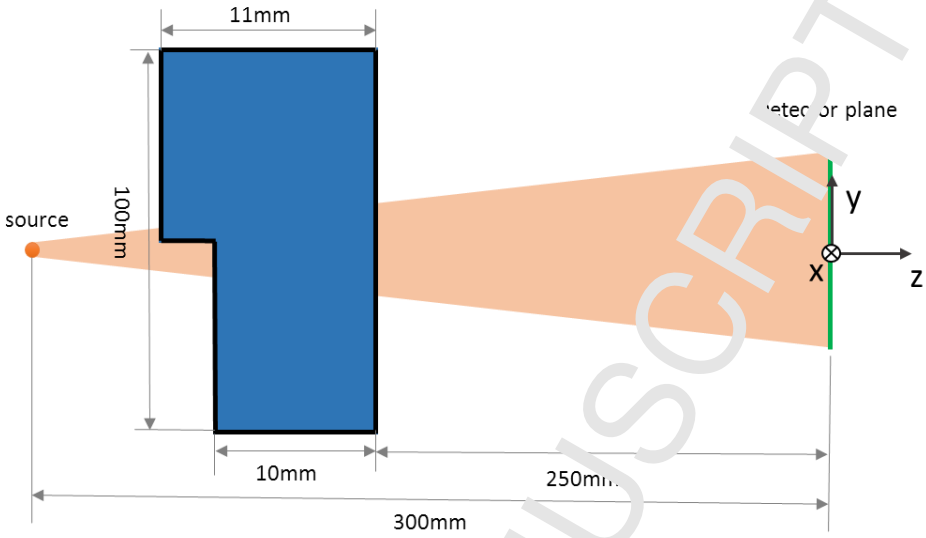

Figure 8: Geometric set-up of the comparison simulation. The object is a two-step iron step-wedge. The detector is a 2 mm × 2 mm × 0.150 mm imaging plate. The beam aperture was set 2/300 rad.

We have simulated the imaging set-up as presented in Figure 8 with a full PENELOPE simulation and our model H1. The source used was a fixed energy cone beam. The energy was 100 keV, and the beam aperture was set to 2/300 rad. The number of the incident photons was 10^9. The PENELOPE simulation running took about 64 hours, we see that the object profile is still noisy, while our H1 model takes about 1 hour including VXI running time and H1 operation time. Note that the comparison was done on a fine scale in order to see the accuracy. Thus, a very fine sampling was used both in spectral and spatial domain:1 keV energy sampling step and a spatial IP sampling with a 100×100×100 grid for x, y, and z directions for a 2 mm × 2 mm × 0.150 mm imaging plate.

Figure 9 presents the object profiles across the iron steps. All profiles have been normalized by their mean signal value. The black one is the object ideal profile. The profile obtained with our *H1* model (blue) agrees perfectly with that obtained with PENELOPE (magenta). The H1 operator being a convolution operator, the profile obtained with our model does not contain any noise, which is normal. This comparison allows to show that the contrast due to the 1 mm step is well modelled by the H1 operator, in comparison with a full MC simulation.

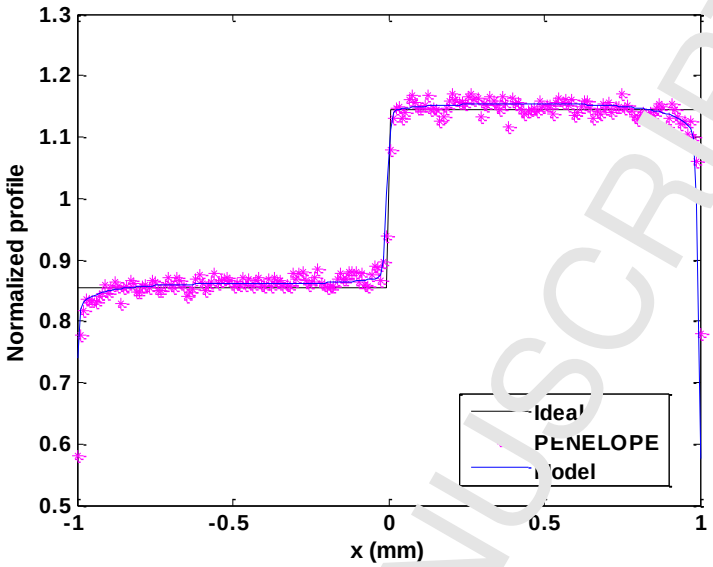

Figure 9: Object grey-level profiles obtained with our *H1* model compared with a full MC simulation (PENELOPE).

5 Result: complex imaging set-up simulation

The model has then been applied to simulate the responses of different detector configurations to the same geometric set-up as illustrated in Figure 3a. A complex shape object with an image quality indicator (IQI) was irradiated by a monochromatic (100 keV) point source. This constitutes a realistic inspection case study where the IQI allows to quantify the image quality in terms of contrast resolution for different hole sizes. The virtual detector was set to 70×70 mm^2 in size with a pixel size of 10×10 μm^2. The photon energy was stored into different energy channels from 1 keV to 100 keV with a channel width of 1 keV.

The detector was modeled as an imaging plate sandwiched between metallic screens. The imaging plate was set as a multiple-layered structure which consists of, in sequence: a 6 µm protective layer, a 150 µm phosphor layer, a 254 µm support layer and a 25.4 µm backing layer. The materials of these layers are respectively Mylar for the protective and support layers, $BaFBr:Eu^{2+}$ for the phosphor layer and polycarbonate for the backing layer.

The responses of the following detector configurations were compared: a) IP alone; b) IP with 0.2mm Pb screens on both sides (denoted as IP+0.2Pb) and c) IP with 0.2 mm Pb and 0.8 mm Sn screens on both sides, where Sn is in contact with IP (denoted as IP+0.2Pb0.8Sn).

Figure 10 presents the full object image accounted by the virtual detector, i.e. the image *Obj(x,y)*. We see the object shape, and the image quality indicator (IQI) in the image center. Then we apply our *H1* model, to obtain the latent image detected with the three detector configurations,

Limg(x,y,z). In order to have a better comparison, we only illustrate the region of interest containing the IQI. Figure 11 compares the IQI zone images obtained using different detectors, where *Limg(x,y)* is obtained by summing *Limg(x,y,z)* over z. Owing to the response of the detector, the signal level drops and the resolution decreases. With the three detectors, the smallest hole can still be identified; however, the sharpness of IP+0.2Pb is not as good as IP alone and IP+0.2Pb0.8Sn. In order to compare the images sharpness, we have normalized the four images to their maximum value. We plot the normalized profiles along AB (see Figure 10) in Figure 12. The sharpness of IP alone is very close to the ideal detector, except a small contrast loss at high spatial frequency (difference at sharp edges). With IP+0.2Pb, the image sharpness is the worst.

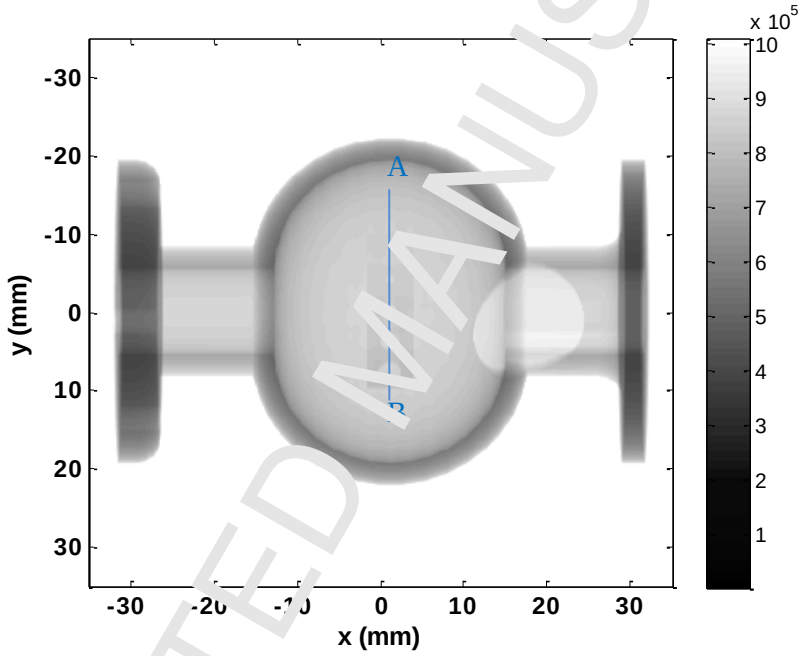

Figure 10: X-ray image obtained with VXI. This 2D illustration is obtained by summing the X-ray image *Obj(E,x,y)* along its energy axis.

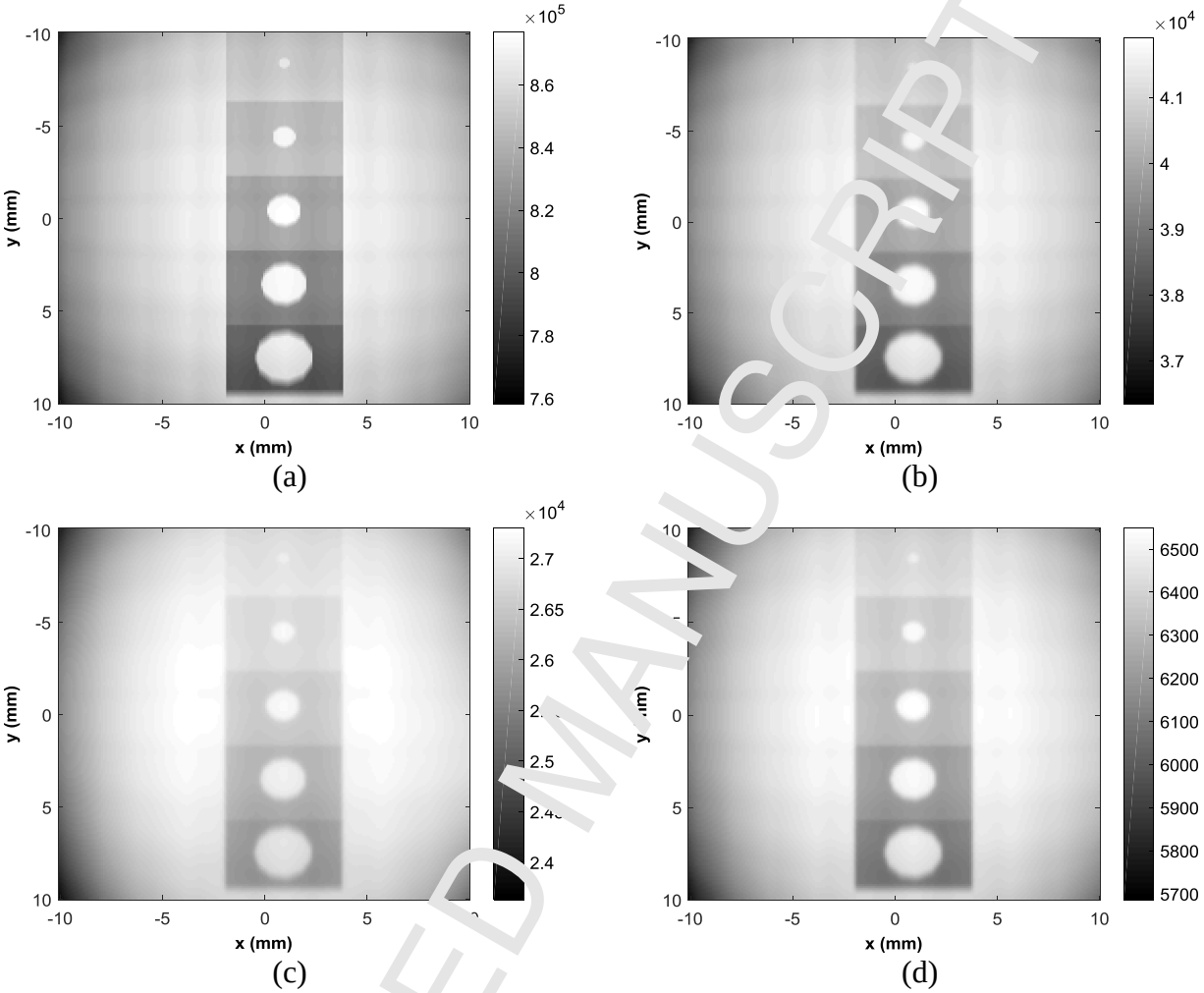

Figure 11: Comparison of the detected image using different detector configurations: a) is the X-ray image *obj(x,y)* b) is the latent image *Limg(x,y)* detected by IP alone using a summation over z direction; c) is the latent image detected by IP with lead screens; and d) is the latent image detected by IP with lead and tin screens.

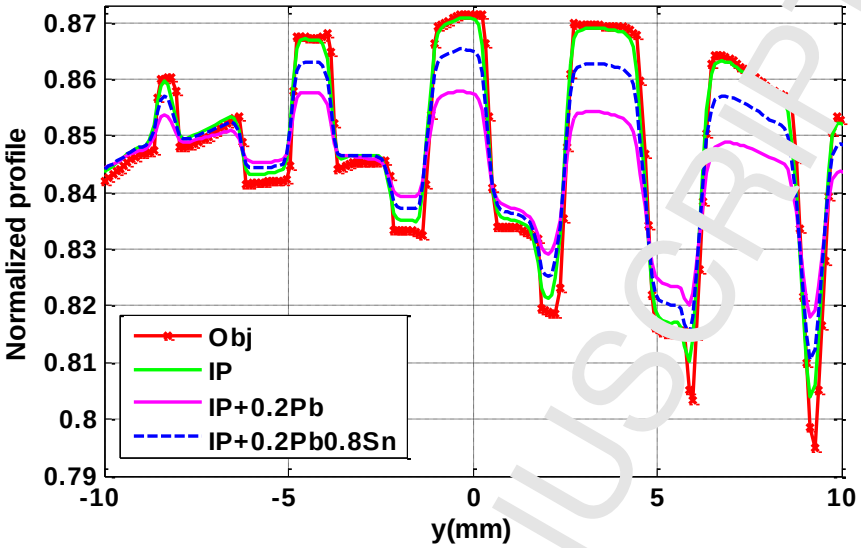

Figure 12: Normalized profiles along the IQI holes (AB line in figure 10): the red curve corresponds to the X-ray image *obj(y)* at the fixed (AB) position; the green, pink and blue curves correspond respectively to the latent image profiles *Limg(y)* obtained with the three detector configurations IP, IP+0.2Pb and IP+0.2Pb0.8Sn.

We then investigated the influence of the readout process on image quality, for one detector configuration. The readout signal depends on the product of the laser power P_{laser} and dwell time t_{scan}, therefore, in the following, we simply use their product as a readout factor $p_{read} = P_{laser} . t_{scan}$.

Figure 13 shows the effect of the optical readout. The images in the upper half are the object image *Obj(E,x,y)* and the energy deposition image in IP alone *Limg(x,y,z)* shown in Figure 11a&b which are reminded here for a better visual comparison. Only a fraction (~ 5%) of the object image is detected by IP. In the lower half, we show the readout images using two different reading factors $p_{read} = 10^{16}$ and $p_{read} = 10^{10}$. With large values of reading power, most of the storage centers can be released (not all the released storage center can contribute to the final image), however a visible shift is observed (comparing Figure 13c&d) due to the scanning process. We focused then on the dependency between the reading efficiency (output signal over input signal) and the laser power (Figure 14). It was observed that the efficiency increases slowly at low laser powers, while a significant rise was pointed out between 10^{13} and 10^{15} p_{read} values; and at 10^{16} the curve starts to reach its maximum. One may notice that the maximum efficiency does not equal to one. Indeed, a high power increases the photoluminescence, but the photons are emitted isotropically and only a small fraction can escape from the front surface of IP and contribute to the final image. In order to compare the image sharpness, the images have been normalized by their maximum values. In Figure 15, profiles along the IQI are presented, along the y direction corresponding to the IP translation direction (with the notations of equations (5)). The red curve refers to the latent image profile. The curves of the first 2 powers overlap each other, then we lose contrast by increasing the power. Comparing the profiles, we also see an obvious shift between the black and the red curves in the IP translation direction due to the scanning process modeled by equation (6).

Thus, the optimum choice of the p_{read} parameter represents a compromise between the need of a large reading efficiency and the care on not degrade the spatial resolution by affecting the neighboring pixels during readout process.

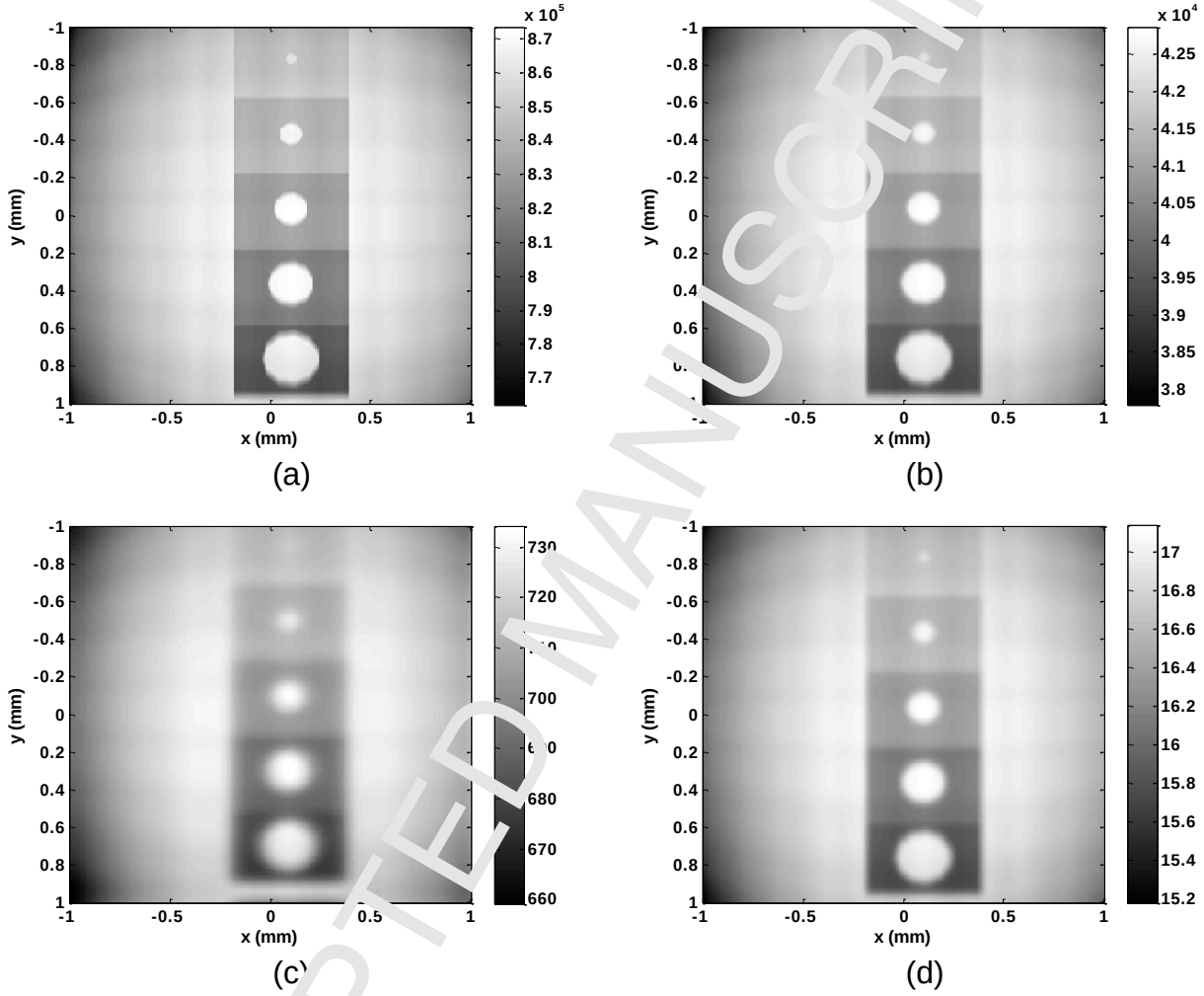

Figure 13: Simulation result: a) object image *obj(E,x,y)*, b) latent image *Limg(x,y)* obtained with IP (same as Figure 11b), c) final *Dimg(x,y)* image with a readout factor $p_{read}=10^{16}$, d) readout factor $p_{read}=10^{10}$.

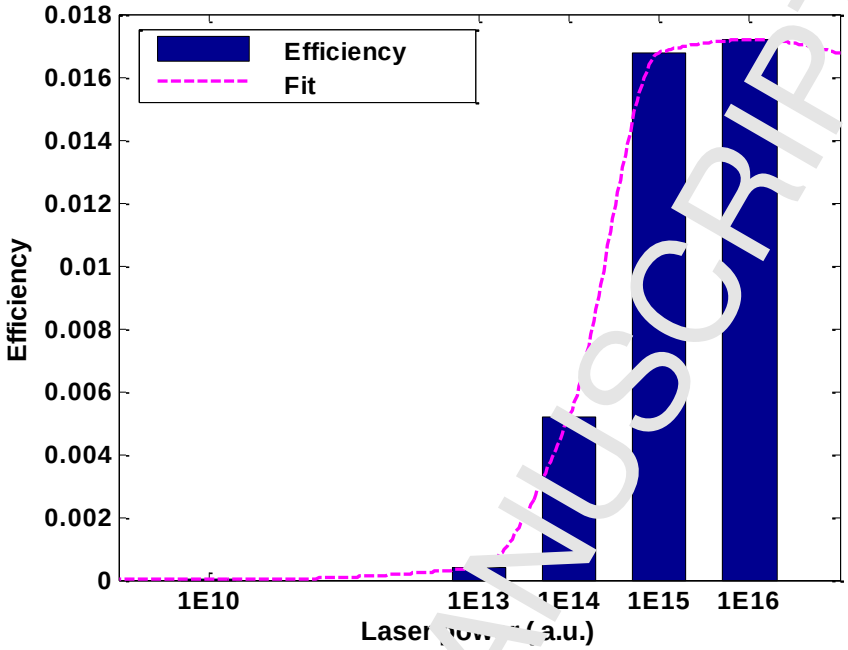

482

483 **Figure 14: Readout efficiency versus laser power.**

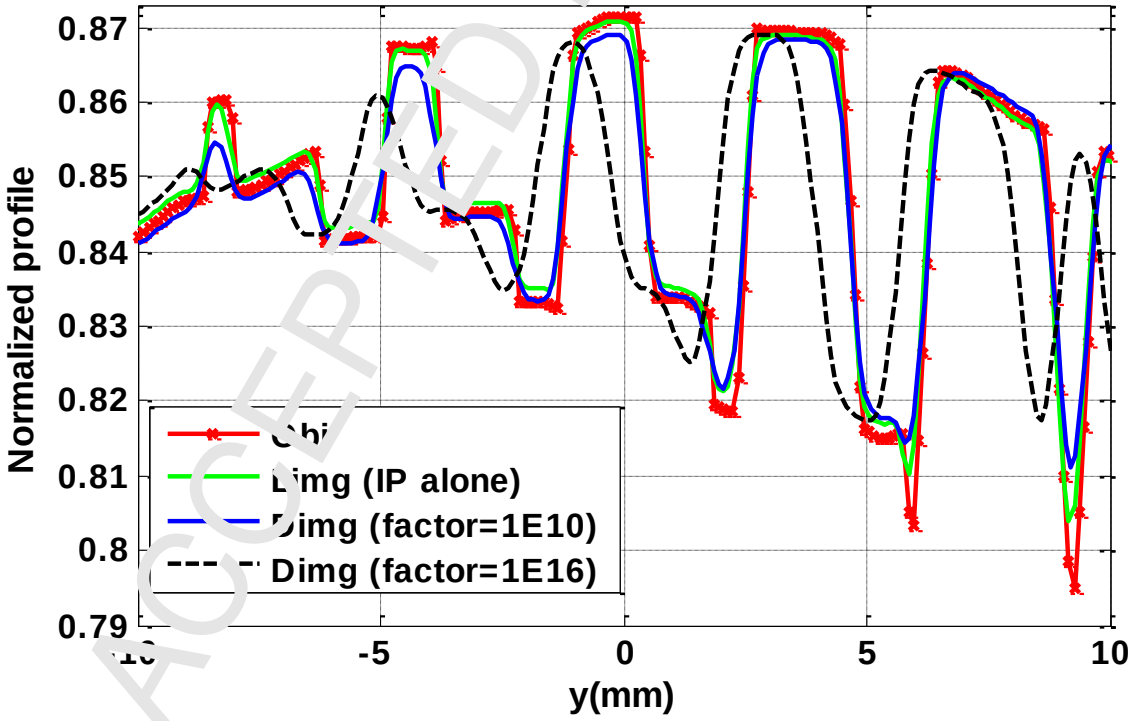

484

485 **Figure 15: Normalized profiles along IQI (line AB shown on figure 10).**

486

6 Discussion and conclusion

This paper presents a CR system model, where the CR detector and the optical readout are modeled as two different transfer functions. As concerns the X-ray exposure part, which is the most crucial step because it conditions the greater part of the final image, the comparison of *H1* operator with the full MC simulation using PENELOPE shows a very good accordance. More details are given in [31] about the optical part simulation which is in good correspondence with [33].

A realistic inspection case study has been defined to illustrate the interest of this full model. As an example, the performances of three different detectors were compared in this particular inspection case. By comparing the obtained images, one can determine the most appropriate detector configuration. Then, different readout factors have been simulated (representing either a change in laser power or a different scanning time), showing the influence on the final image. Increasing the laser power allows to obtain greater signal, although at the expense of spatial resolution. The effect of scanning has been modelled analytically for the first time to our knowledge, and appears as a translation of the image when the readout factor is important.

With this method, one can simulate the complete CR image formation, and take into account the operating factors such as source parameters (in the first step), detector configuration (in the second step) and scanning parameters (in the last step). This full model is "*user-driven*", which means that special emphasis has been taken to the selection of parameters which are accessible to the user (such as laser power). Also a database of 128 detectors has been built thanks to the MC off-line tool, with all physical effects up to energy of 1.4 MeV, which has never been done before. This represents a huge number of simulation hours.

It has to be noted that the application of *H1* and *H2* operators requires the sampling match of *Obj* with *PSFdet* and *Limg* with *f*. Interpolation can be used for this purpose. The computation efficiency strongly depends on the array size of *Obj(E,x,y)*, *Limg(x,y,z)*, *PSF(x,y,z)* and *f(x,y,z)*. Great accuracy requires a small sampling size, and thus a large array size, which makes the simulation slower. The total simulation time varies from minutes to several tens of minutes or even more. It is worth noting that this model does not include noise and allows reasonable simulation time. The user can thus optimize parameters for contrast optimization even for complex shape objects without using noise. However, noise can be added afterwards for a complete image quality assessment.

To summarize, the interests of this global model are:

- Reducing simulation time. The detection efficiency of CR detector at high energy (> hundreds keV) is very small (<1%), therefore, to obtain the same SNR level, a full MC simulation including detector effects would need to generate hundreds times more incident photons than our model H1. Thus, the running is accelerated by at least 100 times.

Using a deterministic code to simulate the object image also reduces the global simulation time.

- Avoiding repeating simulation running. With a full MC simulation, one needs to rerun the MC code for each detector configuration in order to determine the optimal conditions. Thanks to the detector transfer functions, no MC run is needed during the current simulation, as the MC codes are run off-line.
- 3D deposited energy distribution within IP. The CR optical readout is a crucial process that limits the system sharpness and efficiency. The light diffuse along its penetrating depth, hence knowing the 3D deposited energy distribution is important.

The presented simulation code has been successfully applied in a realistic case study with Selenium gamma source in order to compare the image quality obtained using different screens [34].

References

[1] U. Ewert, U. Zscherpel, and K. Bavendiek, "Strategies for Film Replacement in Radiography," in IV Pan-American Conference for Non-Destructive Testing, 2007.

[2] "Non-destructive testing - Industrial computed radiography with storage phosphor imaging plates - Part 2: General principles for testing of metallic materials using X-rays and gamma rays," EN ISO 16 3712-2, 2017.

[3] "Non-destructive testing of welds -- Radiographic testing -- Part 2: X- and gamma-ray techniques with digital detectors," EN ISO 17636-2, 2013.

[4] ASTM Work Item WK34936, Revision of E2033 Standard Practice for Radiographic Examination Using Computed Radiography, ASTM International, 2016

[5] G. A. Mohr and P. Willems, "Factors affecting probability of detection with computed radiography," in 17th World Conference on Non-destructive Testing, 2008, pp. 25–28.

[6] S. Mango, Practical considerations and effects of metallic screen fluorescence and backscatter control in gamma computed radiography, in 19th World Conference on Non-Destructive Testing 2016, http://ndt.net/?id=19253

[7] D. F. Oliveira, J. R. Nascimento, A. S. Machado, C A.Marinho, M. Aiub, J. M. Hohemberger, E. Iguchi, R. T.Lopes Validation of Procedures for Welding Inspection Using Computed Radiography, 11th ECNDT 2014 https://www.ndt.net/search/docs.php3?showForm=off&id=16711

[8] D. W. O. Rogers, "Fifty years of Monte Carlo simulations for medical physics," Phys. Med. Biol., vol. 51, no. 13, pp. R287–301, Jul. 2006.

[9] P. F. Liaparinos, I. S. Kandarakis, D. A. Cavouras, H. B. Delis, and G. S. Panayiotakis, "Modeling granular phosphor screens by Monte Carlo methods," Med. Phys., vol. 33, no. 12, p. 4502, 2006.

[10] J. C. Wagner, D. E. Peplow, S. W. Mosher, and T. M. Evans, "Review of hybrid (deterministic/Monte Carlo) radiation transport methods, codes, and applications at Oak Ridge National Laboratory," in Joint Int. Conf. Supercomput. Nuc. Appl. Monte Carlo, Tokyo, 2010.

[11] S. Vedantham and A. Karellas, "Modeling the performance characteristics of computed radiography (CR) systems," IEEE Trans. Med. Imaging, vol. 29, no. 3, pp. 790–806, Mar. 2010.

[12] C. Kausch, B. Schreiber, F. Kreuder, R. Schmidt, and O. Dössel, "Monte Carlo simulations of the imaging performance of metal plate/phosphor screens used in radiotherapy," Med. Phys., vol. 26, no. 10, pp. 2113–2124, Oct. 1999.

[13] D. S. Brettle and A. R. Cowen, "Dual-energy digital mammography utilizing stimulated phosphor computed radiography," Phys. Med. Biol., vol. 39, no. 11, pp. 1989–2004, Nov. 1994.

[14] G. Barnea et al., "Use of storage phosphor imaging plates in portal imaging and high-energy radiography: The intensifying effect of metallic screens on the sensitivity," Med. Phys., vol. 18, no. 3, pp. 432–438, May 1991.

[15] H. H. Li, A. L. Gonzalez, H. Ji, and D. M. Duggan, "Dose response of BaFBrI: Eu2+ storage phosphor plates exposed to megavoltage photon beams," Med. Phys., vol. 34, no. 1, pp. 103–111, Jan. 2007.

[16] D. A. Jaffray, J. J. Battista, A. Fenster, and P. Munro, "X-ray scatter in megavoltage transmission radiography: Physical characteristics and influence on image quality," Med. Phys., vol. 21, no. 1, pp. 45–60, Jan. 1994.

[17] I. A. Cunningham, M. S. Westmore, and A. Fenster, "A spatial-frequency dependent quantum accounting diagram and detective quantum efficiency model of signal and noise propagation in cascaded imaging systems," Med. Phys., vol. 21, no. 3, pp. 417–427, Mar. 1994.

[18] I. A. Cunningham, J. Yao, and V. Subotic, "Cascaded models and the DQE of flat-panel imagers: noise aliasing, secondary quantum noise, and reabsorption," 2002, vol. 4682, pp. 61–72.

[19] E. M. Souza, S. C. A. Correa, A. X. Silva, R. T. Lopes, and D. F. Oliveira, "Methodology for digital radiography simulation using the Monte Carlo code MCNPX for industrial applications," Appl. Radiat. Isot. Data Instrum. Methods Use Agric. Ind. Med., vol. 66, no. 5, pp. 587–592, May 2008.

[20] S. C. A. Correa, E. M. Souza, A. X. Silva, D. H. Cassiano, and R. T. Lopes, "Computed radiography simulation using the Monte Carlo code MCNPX," Appl. Radiat. Isot., vol. 68, no. 9, pp. 1662–1670, Sep. 2010.

[21] F. K. Koschnick, J. Spaeth, R. S. Eachus, W. G. McDugle, and R. H. Nuttall, "Experimental evidence for the aggregation of photostimulable centers in BaFBr:Eu2+ single crystals by cross relaxation spectroscopy," Phys. Rev. Lett., vol. 67, no. 25, pp. 3571–3574, Dec. 1991.

[22] P. Leblans, D. Vandenbroucke, and P. Willems, "Storage phosphors for medical imaging," Materials, vol. 4, no. 6, pp. 1034–1086, 2011.

[23] P. Duvauchelle, N. Freud, V. Kaftandjian, and D. Babot, "A computer code to simulate X-ray imaging techniques," Nucl. Instrum. Methods Phys. Res. Sect. B Beam Interact. Mater. At., vol. 170, no. 1, pp. 245–258, 2000.

[24] N. Freud, P. Duvauchelle, S. A. Pistrui-Maximean, J.-M. Létang, and D. Babot, "Deterministic simulation of first-order scattering in virtual X-ray imaging," Nucl. Instrum. Methods Phys. Res. Sect. B Beam Interact. Mater. At., vol. 222, no. 1–2, pp. 285–300, Jul. 2004.

[25] M. Yao, P. Duvauchelle, V. Kaftandjian, A. Peterzol-Parmentier, and A. Schumm, "X-ray imaging plate performance investigation based on a Monte Carlo simulation tool," Spectrochim. Acta Part B At. Spectrosc., vol. 107, no. Supplement C, pp. 84–91, Jan. 2015.

[26] F. Salvat, J. M. Fernández-Varea, and J. Sempau Roma, PENELOPE 2008: A code system for Monte Carlo simulation of electron and photon transport : workshop proceedings, Barcelona, Spain 30 June-3 July 2008. Paris : OECD, 2009.

[27] H. von Seggern, "Photostimulable x-ray storage phosphors: a review of present understanding," Braz. J. Phys., vol. 29, no. 2, pp. 254–268, 1999.

[28] J. A. Rowlands, "The physics of computed radiography," Phys. Med. Biol., vol. 47, no. 23, p. R123, 2002.

[29] M. Thoms, "The quantum efficiency of radiographic imaging with image plates," Nucl. Instrum. Methods Phys. Res. Sect. A: Accel. Spectrometers Detect. Assoc. Equip., vol. 378, no. 3, pp. 598–611, Aug. 1996.

[30] M. Thoms, "Image properties of polycrystalline storage films," Appl. Opt., vol. 35, no. 19, pp. 3702–3714, Jul. 1996.

[31] M. Yao, "Computed Radiography System Modeling, Simulation and Optimization," PhD thesis of INSA de Lyon, France, 2014.

[32] L. Wang, S. L. Jacques, and L. Zheng, "MCML—Monte Carlo modeling of light transport in multi-layered tissues," Comput. Methods Programs Biomed., vol. 47, no. 2, pp. 131–146, 1995.

620 [33] R. Fasbender, H. Li, and A. Winnacker, “Monte Carlo modeling of storage phosphor plate readouts,”
621 Nucl. Instrum. Methods Phys. Res. Sect. Accel. Spectrometers Detect. Assoc. Equip., vol. 512, no. 3,
622 pp. 610–618, Oct. 2003.
623 [34] M. Yao, V. Kaftandjian, P. Duvauchelle, A. Peterzol-Parmentier, A. Schumm, "Modeling computed
624 radiography with imaging plates", 19th World Conf. on NDT 2016, Munich,
625 https://www.ndt.net/search/docs.php3?showForm=off&id=19419.
626

Highlights :

We have developed and implemented a novel simulation tool for computed radiography, including not only the X-ray exposure part, but also optical readout.

In order to keep reasonable computing time, all physical effects have been modeled using Monte Carlo code off-line. Two operators have been introduced to then simulate the complete process in an analytic way.

A database of 128 imaging systems (comprised of the phosphor imaging plate and front and back metallic screens) have been modeled.